



# CHORUS

This is the accepted manuscript made available via CHORUS. The article has been published as:

## Generation of high-intensity ultrasound through shock propagation in liquid jets

Gabriel Blaj, Mengning Liang, Andrew L. Aquila, Philip R. Willmott, Jason E. Koglin, Raymond G. Sierra, Joseph S. Robinson, Sébastien Boutet, and Claudiu A. Stan

Phys. Rev. Fluids **4**, 043401 — Published 10 April 2019

DOI: [10.1103/PhysRevFluids.4.043401](https://doi.org/10.1103/PhysRevFluids.4.043401)

# Generation of high-intensity ultrasound through shock propagation in liquid jets

Gabriel Blaj,<sup>1</sup> Mengning Liang,<sup>2</sup> Andrew L. Aquila,<sup>2</sup> Philip R. Willmott,<sup>2,3</sup> Jason E. Koglin,<sup>2</sup>  
Raymond G. Sierra,<sup>2,4</sup> Joseph S. Robinson,<sup>2</sup> Sébastien Boutet,<sup>2</sup> and Claudiu A. Stan<sup>4,5,\*</sup>

<sup>1</sup>*Technology Innovation Directorate, SLAC National Accelerator Laboratory, Menlo Park, CA 94025, USA*

<sup>2</sup>*Linac Coherent Light Source, SLAC National Accelerator Laboratory, Menlo Park, CA 94025, USA*

<sup>3</sup>*Paul Scherrer Institute, CH-5232 Villigen, Switzerland*

<sup>4</sup>*Stanford PULSE Institute, SLAC National Accelerator Laboratory, Menlo Park, CA 94025, USA*

<sup>5</sup>*Department of Physics, Rutgers University Newark, Newark, NJ 07102, USA*

(Dated: March 22, 2019)

We investigated the generation and propagation of ultrasonic pressure waves produced by focused X-ray free-electron laser pulses in 14 to 30  $\mu\text{m}$  diameter liquid water microjets. The pressure waves formed through reflections, at the surface of the microjets, of the initial shock launched in the liquid by the X-ray pulse. These waves developed a characteristic geometric pattern which is related to, but different from, the shock structures of supersonic gas jets. Fully developed waves had initial peak pressures ranging from less than  $-24$  MPa to approximately 100 MPa, which exceed the compressive and tensile strengths of many materials, and correspond to extreme sound intensities on the order of  $1 \text{ GW/m}^2$  and sound pressure levels above 270 dB (re:  $1 \mu\text{Pa}$ ). The amplitudes and intensities were limited by the wave destroying its own propagation medium through cavitation, therefore these ultrasonic waves in jets are one of the most intense propagating sounds that can be generated in liquid water. The pressure of the initial shock decayed exponentially, more rapidly in thinner jets, and the decay length was proportional to the jet diameter within the accuracy of measurements. Extrapolating our results to thinner jets, we find that the pressure waves may damage protein crystals carried by liquid jets in X-ray laser crystallography experiments conducted at megahertz repetition rates.

---

\* Email: claudiu.stan@rutgers.edu

## I. INTRODUCTION

Sound, defined as a propagating pressure wave with multiple positive and negative swings around an equilibrium pressure, has a maximum possible amplitude that is limited by the capacity of the transmitting medium to sustain the pressure peaks and return to its equilibrium pressure undamaged, meaning that properties such as its phase do not change. For example, sound amplitude in a gas is limited at the low peak by absolute zero pressure and at the high peak by the condensation pressure. The low pressure peak in condensed materials can have absolute negative values since solids and liquids can support mechanical tension or negative pressures. In liquids, the largest possible sound amplitude is typically limited by cavitation at negative pressures, because many liquids can be compressed dynamically to much larger pressures[1] than the absolute pressures[2] at which cavitation occurs.

Sound that approaches its maximum possible amplitude is important both practically and scientifically. For example, high-amplitude sound also has high intensity and carries large amounts of energy, which can be useful for communication at long distances. In nature, loud sounds produced in water by aquatic animals may be used to echolocate small prey at large distances[3]. Air-propagating sound with very high intensities, such as rocket engine noise[4], can be damaging to structures and the environment thus measures are taken to reduce its level[5]. High amplitude sound becomes a nonlinear wave, and is important due to the nonlinear phenomena it induces[6].

To our knowledge, the largest peak-to-peak pressures reported for sound in liquid water initially at atmospheric pressure (0.1 MPa) were generated using focused ultrasonic waves[7]. These studies focused on cavitation and achieved pressure swings from approximately +30 to -30 MPa, corresponding to peak-to-peak pressures around 60 MPa, and reaching the regime where the sound is limited by failure (cavitation) of the transmitting medium. In theory, the maximum pressure swing for sound in water is given by the negative pressure at which the homogeneous nucleation of cavitation occurs (-120 to -140 MPa)[8, 9], but water has a complex cavitation behavior[10] and in ultrasonic experiments cavitation is observed at pressures near -30 MPa[7, 11].

A sufficiently strong pressure wave becomes a shock wave[12, 13], but while liquids can withstand shock pressures of tens of GPa before solidifying[1], the techniques used to make shocks generally cannot produce multiple shocks that would generate a periodic pressure wave. Shock trains can be however generated though the reflection of shocks at the boundaries of the system, for example the Mach discs formed in the exhaust of jet engines into open atmosphere[14], or the shock trains that form during supersonic gas flow in ducts and tubes[15].

Here, we show that shock trains can also be generated in free liquid microjets, by an initial shock generated by a focused femtosecond X-ray laser pulse. Unlike the shock trains in gases, the ones in liquid jets reached large negative pressures that led to cavitation. We estimate that the amplitudes of these pressure waves exceed the largest peak-to-peak pressures obtained with focused ultrasonic waves, and may thus be the highest intensity sounds generated to date in liquid water.

## II. EXPERIMENTAL DESIGN

Figure 1 shows the experimental setup we used at the CXI instrument[16] at the Linac Coherent Light Source (LCLS) X-ray free-electron laser (XFEL)[17]. Liquid water microjets with diameters of 14.4, 20.2, and 30  $\mu\text{m}$  were injected into a vacuum chamber (pressure  $< 1$  Pa), where they were intercepted by focused X-ray pulses (9.5 keV photon energy, pulse energy on the order of 1 mJ, 40 fs pulse duration, 1.3  $\mu\text{m}$  nominal beam diameter at full width half maximum). The absorption of X-rays under these conditions is weak and linear[18], and less than 0.02 of the XFEL pulse energy was absorbed in the region of the jet illuminated by X-rays.

The interaction between the XFEL pulse and the jet leads, as illustrated in Fig. 1, to ultrafast ionization and heating of the illuminated region[19], vaporization of the liquid, and the formation of a cylindrical shock wave in the liquid[20], which later propagates along the jet[21]. To observe the shock waves, we used time-resolved optical microscopy with illumination from a femtosecond pulsed optical laser[20, 21]. An in-vacuum microscope with a 50 $\times$  long-working distance objective (Mitutoyo) and a high-speed camera (Phantom Miro M340, Vision Research), produced images with a magnification of 0.2  $\mu\text{m}/\text{pixel}$  and an optical resolution better than 0.78  $\mu\text{m}$ . Due to the refraction of light inside the jet, the images are magnified[20, 22] in the direction perpendicular to the jet by a factor of  $\approx 1.33$ . Therefore, if the images display the interior of the jet all the way to the jet edge, only regions up to  $\approx 0.75$  of the jet diameter are actually imaged.

The propagation of shocks was determined using a pump-probe technique, by recording single images of the jet at delays ranging from -20 to 37 ns relative to the arrival of the XFEL pulse. During the experiment, the delay of the optical laser was scanned continuously over the delay range while recording one jet image for each XFEL pulse. As the shock properties depend on the energy of X-ray laser pulse, which varies randomly shot-to-shot[23], only data corresponding to a  $\pm 5\%$  band around the most probable pulse energy in a data set was selected for further analysis. The pulse energies were determined as relative values for each pulse, by measuring the X-ray scattering from the jet

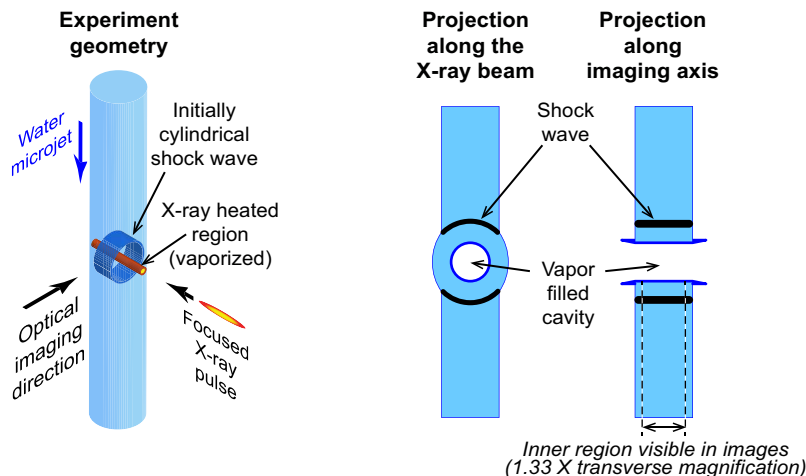


FIG. 1. Experiment schematic. A water microjet is intercepted by a focused X-ray laser pulse that launches an initially cylindrical shock wave in the liquid. To observe the propagation of shock and pressure waves, the jet is imaged orthogonal to the jet and the X-ray pulse.

onto a single tile of a 2D X-ray detector[24, 25] placed along the beam after the jet. The absolute energy of each pulse was also recorded just after the X-ray generation (i.e. at the XFEL source), however this data was less precise than the X-ray detector measurement because of the beam position jitter[23], which induces shot-to-shot variations in the attenuation of pulses between the source and the sample. We used the absolute measurements to report the average pulse energy in a data set, and the relative measurements for single-shot data sorting. We note that the energy of the pulses interacting with the jet is smaller than the absolute measurements reported here; we estimate that the XFEL pulse was attenuated by a value between 2 and 4 before arriving at the jets.

### III. RESULTS AND DISCUSSION

We investigated in detail the propagation of shocks and the generation of multiple-cycle pressure waves in jets with diameters of 14.4 and 20.2  $\mu\text{m}$ , using either full-energy XFEL pulses, or pulses attenuated to  $\approx 25\%$  of their initial energy. Four different data sets were recorded, each containing more than 1000 images. Approximately one quarter of the images were assembled into four movies that display all the relevant phenomena associated with the wave propagation (see the Supplementary Materials[26]). Complete, full-resolution image data sets and associated metadata are available from a data repository[27]. We also recorded images of 30- $\mu\text{m}$  jets intercepted by full-energy pulses[26], using a ten-fold larger field of view, to observe the features of the pressure wave propagation at distances up to  $\approx 1$  mm.

In the images, shock waves are visible due to the difference in refractive index between the pre-shocked liquid and the shocked liquid. The refractive index difference can either bend the illumination light outside the numerical aperture of the objective and make the shocks visible as dark lines, or reflect additional light into the objective, case in which the shocks appear as bright lines. Due to the small diameter of the jets, the optical contrast of the shocks was weak, and the images were processed to increase their contrast[26].

#### A. The formation and dynamics of the pressure waves in jets

All the data sets exhibited the same wave generation and propagation dynamics, but the dynamics were more visible in larger jets and at larger pulse energies. Figure 2 shows images illustrating the main features of this dynamics for a 20.2- $\mu\text{m}$  jet and full-energy pulses. The shock and the cavity became visible only 1–2 ns after the XFEL pulse, because the initial ultrafast heating creates a pressure distribution that reflects the X-ray intensity distribution with smaller values in the outer regions, and the pressure wave must propagate for a finite distance until the increase of sound velocity with pressure leads to the formation of a shock discontinuity. The initial shock interface was straight, as expected when projecting a cylindrical wave onto a perpendicular imaging direction.

At  $\approx 5$  ns time delays, the shock started to curve, followed by the appearance, at  $\approx 10$  ns, of a triangular dark region. The triangular dark region became smaller after  $\approx 20$  ns, and previous experiments (see the supplementary materials

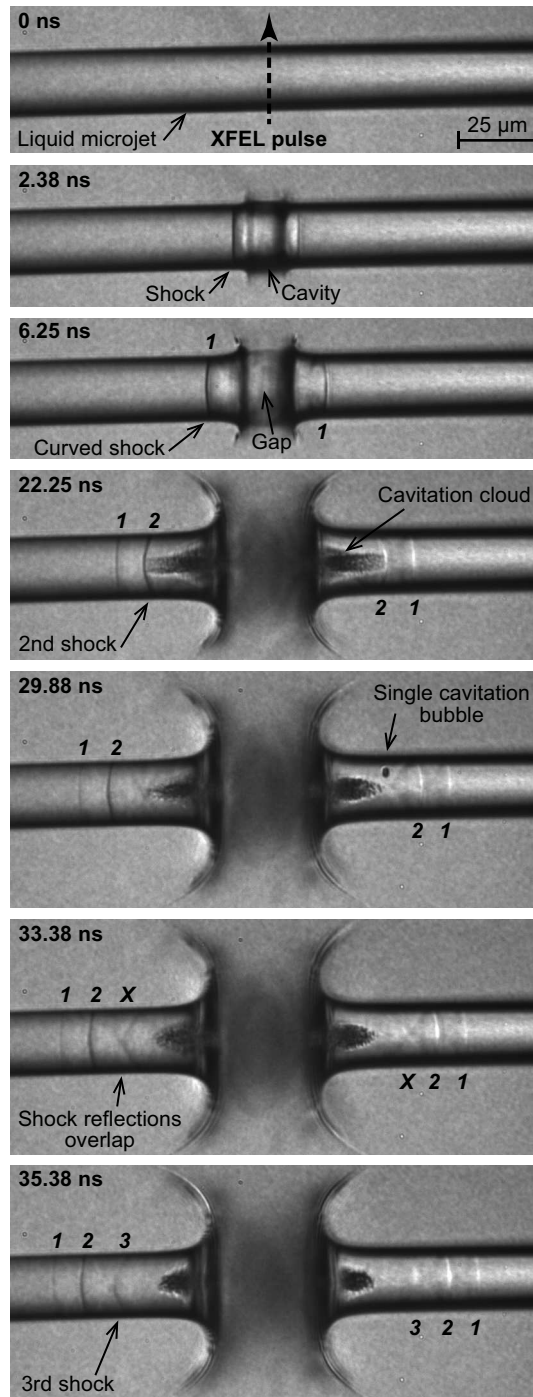


FIG. 2. Generation and propagation of the pressure wave. The images show how after the generation of an initial shock by the XFEL pulse (1.7 mJ at source) in a 20.2- $\mu\text{m}$  water jet, additional shocks and pressure oscillations develop. Two types of cavitation occurred: a cavitation cloud, and single cavitation bubbles.

of Ref. [21]) showed that the dark region fully disappears at  $\approx 100$  ns. The small dots observed at the tips of the dark region, as well as its rapid appearance and disappearance, indicate that it is a cavitation cloud made from many bubbles with sizes close to or below the optical resolution – same as the cavitation clouds observed in laser-induced microfluidic cavitation experiments[28]. These small bubbles collapse rapidly because the water vapor pressure (2–3 kPa near room temperature) is smaller than the capillary pressure ( $\approx 300$  kPa for a 1-micron diameter bubble).

The cavitation cloud shrunk gradually without the oscillations and rebounds characteristic to single bubble collapse[29]. Millimeter-sized dense cavitation clouds also shrink gradually[30], thus gradual collapse may be charac-

teristic of dense formations of cavitation bubbles. Nevertheless, we cannot rule out cloud oscillations that start with random phases or frequencies, since they would not be detectable in a pump-probe experiment.

At  $\approx 20$  ns, a sharp line indicative of an additional pressure jump (the second shock) appeared between the cavitation cloud and the initial shock wave (the first shock). Further pressure discontinuities continued to appear at longer delays; previously[21], up to 6 visible pressure discontinuities were observed in a 20- $\mu\text{m}$  jet at time delays of  $\approx 250$  ns and propagation distances of  $\approx 400$   $\mu\text{m}$ . Here we observed up to 6 pressure modulations in a 30- $\mu\text{m}$  jet at a time delay of 606 ns and a propagation distance of 885  $\mu\text{m}$  (see Figure S3 in [26]). Consecutive pressure modulations (i) were separated by distances proportional to the jet diameter, (ii) these distances increased with the modulation number, and (iii) they remained approximately constant during the propagation of the wave. The distance between the first and the second shock was equal to approximately 0.4 jet diameters in all data sets and increased to 0.6 jet diameters between the 5<sup>th</sup> and the 6<sup>th</sup> modulations observed at 606 ns delay. A wave with six pressure cycles thus had a variable frequency  $f$  given by

$$\frac{u_s}{0.6 D} < f < \frac{u_s}{0.4 D} \quad (1)$$

where  $u_s$  is the speed of the wave and  $D$  is the jet diameter. Approximating the speed of the wave with the speed of sound in water,  $\approx 1500$  m/s, the center frequency of  $u_s/(0.5 D)$  ranged between  $\approx 100$  MHz (30- $\mu\text{m}$  jets) and 200 MHz (14.4- $\mu\text{m}$  jets).

The image sequence shown in Fig. 2 ends before the third shock was fully formed. The bottom images show faint dark lines that trail the second shock and intersect in the middle of the jet; the third shock will form at the crossing of the lines. The complete formation of the third shock is however visible in the data for 14.4 micron jets (see [26]).

## B. The mechanisms of cavitation and shock train generation

The liquid jet is a wave-conducting medium with fully compliant walls. Supersonic gas jets ejected into another gas at atmospheric pressure, such as the ones generated by jet and rocket engines, are also a wave conduit with compliant walls. The wave structures and shock trains that form in gas jets, first reported in 1890 by Mach and Salcher[31], are a well studied problem[14, 32]. If the pressure in the gas jet is different from the atmospheric pressure, compression or rarefaction waves are generated at its boundary and travel across the jet. Since the jet is also moving, these waves form crisscrossing patterns that can exhibit rhombic regions (Mach diamonds), or repeated shocks (Mach discs). In gas jet experiments the jets are moving supersonically and the shocks are stationary in the reference frame of the gas nozzle, while in our experiments the shocks propagate in an approximately static jet; however, snapshot images of the shock structures are independent of the frame of reference. Many features of the shocks in gas jets are similar to the ones we observed in liquid jets, and provide useful analogies. The gas jet phenomena can be explained graphically by constructing the wave fronts of the various reflections[32], and here we took the same approach to explain shock propagation in liquid jets.

Figure 3 illustrates schematically the physical processes leading to cavitation and the generation of secondary shocks, which are both caused by the reflection of pressure waves at the surface of the jet. Pressure waves arriving at the jet surface must produce reflected waves in order to satisfy the boundary condition for the pressure, which in our case is equal to the vacuum chamber pressure and thus negligible. Thus, a positive-pressure incoming wave generates a negative-pressure reflected wave to cancel the pressure at the surface. For example, a plane positive pressure wave reflected normally at a water-vacuum interface (incidence angle  $0^\circ$ ) will generate a reflected wave with a negative amplitude equal in absolute value with the pressure of the incoming wave[33].

Oblique reflections of shocks (incidence angle  $> 0^\circ$ ) are more complicated. Regular reflections, where the incident and reflected waves propagate straight and meet on the surface, are not always possible and multiple cases of wave distortion exist depending on the acoustic impedances of the two materials [34, 35]. In the case of shocks arriving from water at an interface with air or vacuum, a shock incoming at an angle smaller than a critical angle can generate a reflected expansion wave with multiple components propagating at different angles, forming a rarefaction fan[34]; this is still a regular reflection. At incidence angles larger than the critical angle regular reflections are not possible. For this reason, a plane shock launched perpendicular to the axis of the liquid jet cannot remain flat and meet the jet surface at a  $90^\circ$  (grazing) incidence angle. Instead, the shock curves where it meets the surface, such that the incidence angle becomes less than  $90^\circ$  and an oblique shock reflection occurs (see for example Figs. 18, 19 in Ref. [35]). An additional complication arises from the curvature of the jet's surface, which may focus[20] reflected waves.

Despite the complexity of the shock reflections, the major features shown in Fig. 2 can be understood qualitatively. Figure 3(a) illustrates the formation of the cavitation cloud assuming the shock reflections are regular. If the initial shock pulse has a length smaller than the jet diameter, its reflections can separate spatially from the initial shock and become negative pressure pulses, whose overlap leads to the generation of large negative pressures and to cavitation.

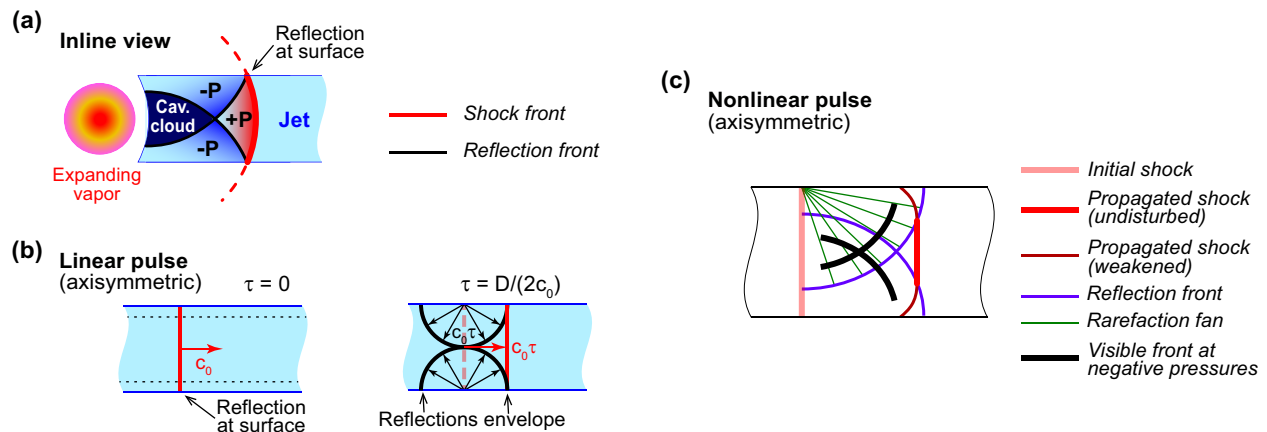


FIG. 3. Qualitative description of the phenomena induced by the initial shock. (a) Reflection of the initial shock at the surface of the jet generates negative pressure reflections that overlap and generate sufficiently large tensions to form a cavitation cloud. (b) Huygens-Fresnel construction of reflections from a linear plane pressure pulse propagating in a jet, showing that the closest place where all the reflections overlap trails the shock at one half of the jet diameter. (c) A nonlinear high-pressure pulse generates a rarefaction wave that catches up with the shock and weakens it, leading to a curved shock interface. The amplitude dispersion of the reflected wave’s velocity generates a delayed pressure jump that becomes visible in the images.

The geometrical construction in Fig. 3(a) also illustrates the expected shape of the positive pressure pulse, which is similar to the triangular shape visible in the images.

The new shocks form where the reflections intersect on jet axis, either at the tip of the cavitation cloud, or at the region marked “X” in Fig. 2. Figure 3(b) explains the approximately one-half diameter spacing of shocks using the Huygens-Fresnel principle applied to the perturbation that is generated by the surface reflections, because what we observe in images is the perturbations that are superimposed on a plane shock advancing in the jet. As the first shock reaches the surface of the jet, the perturbation generated by the reflected wave is constructed as a superposition of spherical waves originating from all the points where the plane shock intersects the surface[36]. The envelope of all reflections is given by the reflections that occurred at the first time considered ( $\tau = 0$ ): since in Fig. 3(b) we use a linear approximation all waves propagate with at the speed of sound and waves generated by later reflections ( $\tau > 0$ ) remain enclosed within the envelope of the first reflection. The closest location where all the reflections overlap is on the symmetry axis of the jet, trailing the first shock by one-half of the jet diameter. The reflections of a stronger shock will trail the first shock closer, because the speed of sound inside a shock-compressed material is larger than the shock wave velocity[12, 13]; nevertheless, the reflection fronts generated by a stronger shock are still defined by the  $\tau = 0$  reflection because the reflection points move in the lab frame at the shock velocity, which is smaller than the speed of sound in the shock-compressed material[13].

If only the wave reflections at surface are considered, the formation of new shocks at the crossing of reflections is counterintuitive. Since pressure wave reflections at a liquid-vacuum interface lead to a change in the sign of pressure, two wave reflections (positive-to-negative, then negative-to-positive) are required for a positive-pressure shock. Using the wave construction shown in Fig. 3(a), the second reflection would then start when the envelope touches the opposite side of the jet, at twice the time delay shown in the figure, and leading to a spacing between the first and the second shock of at least one jet diameter. Shock structures with a wavelength of one jet diameter or more are encountered in supersonic gas jets [14, 32], but in the liquid jets we observed a wavelength of approximately half the jet diameter (see Eq. 1), corresponding to a roughly doubled frequency relative to supersonic gas jets. It thus appears that a “frequency doubling” process occurs in liquid jets. A related feature is that the wave structure that is visible in liquid jets can be described as triangles that have the base at the shock line and the tip pointing against the direction of propagation, approximately in contact with the following shock. These triangles can be thought as one half of the geometrical shape of Mach diamonds[14] in supersonic gas jets, and in analogy we can call them “Mach triangles”; they are most easily visible in the supplementary movies[26].

The formation of the second shock offers insight into why shocks form at the crossing of reflected waves rather than after two surface reflections. The second shock forms just ahead of the cavitation bubble cloud, where the expansion of bubbles reduces the negative pressures towards zero pressure. Even if the peak pressure behind the second shock is approximately zero, a shock wave can still form if the pressure just ahead of it is lower and thus negative, because the compressibility and the speed of sound of water continue to decrease down to at least  $-137$  MPa[37–39]. Thus, the initial pressure distribution of the first two shocks is likely to be similar to the N-wave sonic boom profiles[40] produced by supersonic aircraft, where the initial pressure jump at the head of the boom (from atmospheric pressure

to high pressure) is followed by another pressure jump at the tail of the boom (from low pressure to atmospheric pressure). A single surface reflection is enough to generate a trailing shock because cavitation provides a relatively high pressure region at the tail of the reflection, which develops into a new shock.

After the formation of the second shock, the wave separates from the cavitation cloud, and new fronts continue to be generated. Although the cavitation cloud plays a role in the formation of the second shock, it cannot play a role in the formation of new shocks because in order to catch up with the propagating wave the cloud should generate highly supersonic pressure modulations; such supersonic modulations are also high pressure shocks that would be visible experimentally. We did not observe cavitation bubbles or clouds of bubbles at the delays and locations where the third and higher order fronts developed. It is unlikely that bubbles too small to be imaged form under such conditions and drive the generation of new fronts: nucleation rates for cavitation depend very steeply on pressure, therefore it is unlikely that bubbles are always generated in the right amount as the pressure of wave, as it will be shown below, varies by more than one order of magnitude; also, this process should operate similarly in jets with different diameters and thus different time scales for the wave dynamics.

Instead, the formation of new fronts in the absence of cavitation may be caused by the steepening of the pressure wave after it achieves its most negative pressure, process which should generate a shock similar to the tail shock in sonic booms. We have observed previously that XFEL-induced negative pressure waves in droplets develop a visible front that lags the outer front of the wave, and this front could be a tail shock (see the supplementary text of Ref. [20]). For the jet experiments, Fig. 3(c) shows the corresponding position of the visible front lagging behind the outer wave front. If the visible front is a tail shock, the crossing of the fronts is an oblique shock reflection, and if the reflection is irregular it will merge the shocks into a single one (a Mach disc)[32], because in this case the reflected wave is also a shock, and it combines constructively with the incident shock. This process is consistent with our experimental observations, therefore we hypothesize that the formation of tail shocks and their merging in an irregular reflection is the last step in the formation of a new shock in the jet.

The curving of the shock front at delays longer than 5 ns is illustrated in Fig. 3(c). The reflections generated by the first shock travel in the shock-compressed material faster than the shock[13] and catch up with it; the superposition of the shock and its reflection decreases the amplitude of the initial shock and thus its velocity, generating a backward-curved shock formed by the superposition of the incident and reflected waves [35]. Shock front curving was observed experimentally after reflections at air-CO<sub>2</sub> interfaces[41], and in numerical simulations of shocks arriving at water-air interfaces[35].

### C. The positive peak pressure of the wave and its decay

The jump in pressure due to the first shock can be calculated from its velocity of propagation, because for a given pressure and temperature, the relation between shock wave pressure and velocity is a property of the material. Experimental measurements of this relation are available for liquid water at ambient conditions[42, 43], and are applicable to our experiments in vacuum because the atmospheric pressure is much smaller than the pressure jumps. We cannot, however, use velocity-pressure relations to measure the pressure jumps in the subsequent trailing shocks, because our experiment does not provide the pre-shock pressures, which may have large positive or negative values comparable in absolute value to the pressure jump of the shock.

The pressure jump due to a shock wave,  $P_S$ , is given[13] by

$$P_S = \rho_0 c_S u_p \quad (2)$$

where  $\rho_0$  is the initial density of the material,  $c_S$  is the shock velocity, and  $u_p$  is the particle velocity in the shock. Eq. 2 is an exact relation derived from conservation laws[13]. We used a simple approximation for the shock velocity  $c_S$ , [43, 44]

$$c_S = c_0 + B u_p \quad (3)$$

where  $c_0$  is the speed of sound and  $B$  is a numerical coefficient that has a value close to 2 for shocks in water.

Because the jets were injected in vacuum, the liquid cooled through evaporation. We calculated the temperature distribution inside the jets at the interaction region using an evaporative cooling model for droplets[45], which we modified for a jet with uniform flow velocity distribution[26]. We used an evaporation coefficient  $\gamma = 1$  as used and confirmed by recent experiments[46, 47], and we neglected that the jet exits the nozzle with an initially nonuniform velocity distribution due to viscosity, which lowers the cooling rate in the center of the jet[48]. The jet regions near the symmetry axis, where we made the shock velocity measurements, have approximately constant temperatures around

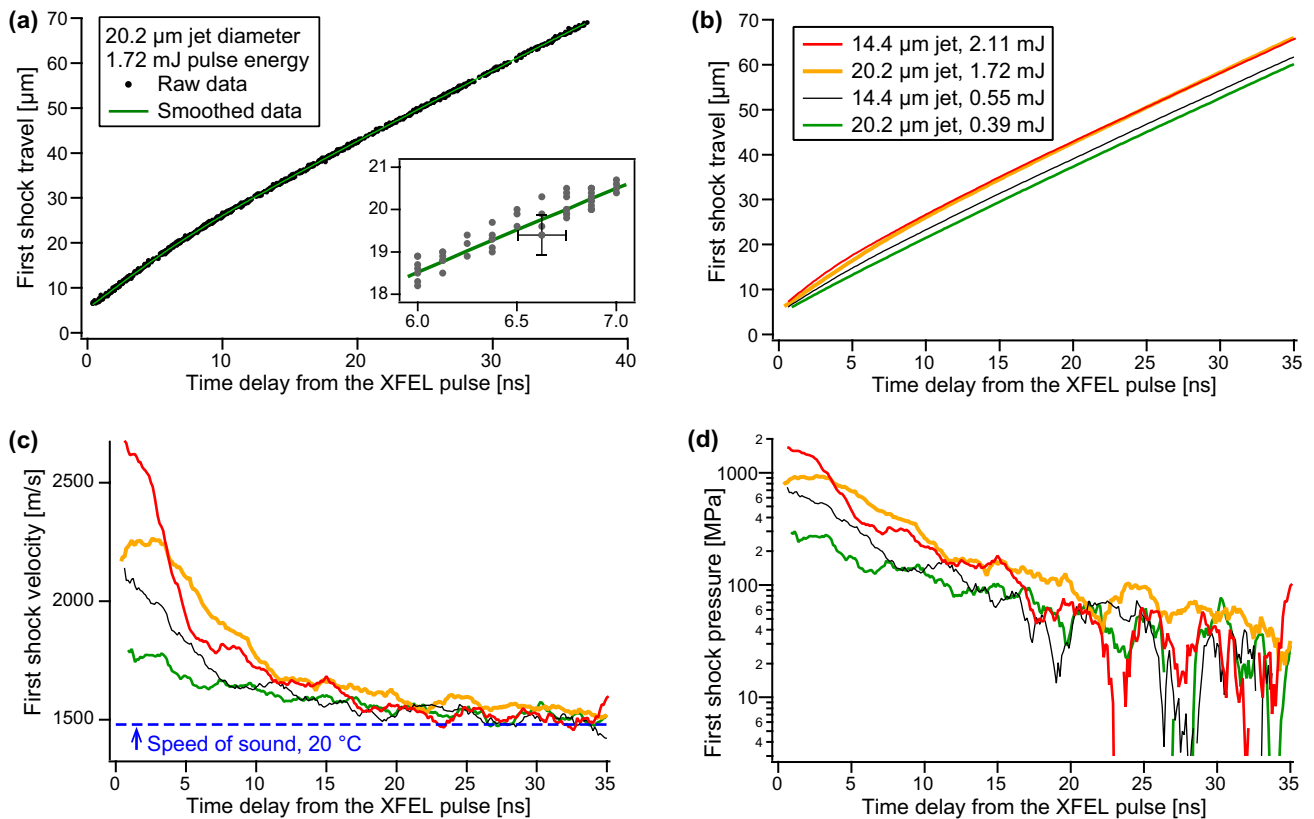


FIG. 4. The kinematics and pressure of the first shock wave. (a) Raw shock position data for one data set and corresponding smoothed data. (b) Smoothed shock position for all data sets. (c) Velocities of the first shock. (d) Pressures of the first shock. The data sets have the same line color and type in the panels b)–d).

21 °C in the 20.2- $\mu\text{m}$  jets and 19 °C in the 14.4- $\mu\text{m}$  jets. Since shock pressure-velocity measurements made exactly at these temperatures are not available, we used in Eq. 3 a temperature-dependent speed of sound,  $c_0(T)$ , using the fit given by Petiet *et al.*[49], and we expressed the temperature dependence of the numerical coefficient  $B$  through a linear interpolation of measurements[43, 44] done at 0 and 25 °C:  $B(T) = 2.1035 - 0.010368 \times T$ , where  $T$  is the temperature in degrees Celsius. Combining Eqs. 2 and 3, we calculated the shock pressure jump from measurements of  $c_S$  using

$$P_S = \rho_0(T)c_S \frac{c_S - c_0}{B(T)} \quad (4)$$

We estimate that Eq. 4 can be applied to our data with a  $\pm 5\%$  accuracy, because up to 15 GPa it reproduces within 5% Rice and Walsh’s data for liquid water at 20 °C[42].

Figure 4(a) shows the position of the first shock as a function of the delay time, for a 20.2- $\mu\text{m}$  jet and a 1.7 mJ pulse. As this raw data is too noisy to extract the shock velocity by direct numerical derivation, we have smoothed it using Savitzky-Golay filtering[50], which we implemented as least-square linear fits of data in a  $\pm 2$  ns time window (see [26] for details). The filtered position data, shown in Fig. 4(b) for all four conditions investigated, was then used to calculate the velocity and pressure of the first shock.

Figure 4(c) shows the shock velocity calculated by differentiating the filtered data, and Fig. 4(d) shows the shock pressure derived from the shock velocity. The velocities are larger than the speed of sound, as expected for a shock, but they decrease rapidly and after  $\approx 20$  ns the velocity noise becomes comparable to the difference from the speed of sound. The noise in the data is caused by biases in the shock position measurements, due to local variations in background brightness caused by laser speckles[26].

The initial pressures of the first shock ranged from 0.3 to 1.5 GPa and are roughly proportional to the X-ray pulse energy (see Fig. S5 in [26]). Later, the decay of the shock pressure is more rapid in the thinner jets, as seen by the crossing of the position and pressure curves in Fig. 4. Since the decay of shocks is related to the shock reflections,

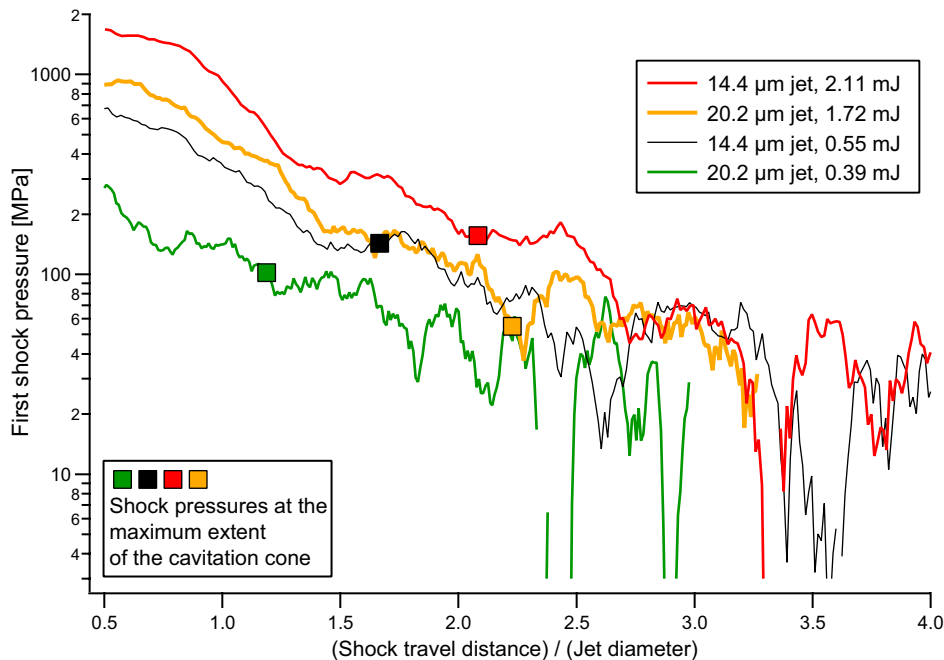


FIG. 5. Attenuation of the first shock with the propagation distance scaled by the jet diameter. The shock initially decays with approximately the same exponential decay law for all data sets. When the shocks arrive at the maximum extent of the cavitation cloud, they have a pressure around 100 MPa for all conditions investigated.

and the frequency of these reflections is inversely proportional to the jet diameter (Eq. 1), the initial decay of the first shock should also scale with the inverse of jet diameter and be more rapid in thinner jets.

Figure 5 shows the peak pressure of the first shock as a function of the propagation distance scaled by the jet diameter. When the propagation distance is scaled, the relative decay of pressure is similar at short propagation distances for all data sets.

#### D. Negative pressures in the propagating wave

Negative pressures in the jets are expected after the reflection of shocks at the jet surface, but an accurate calculation of their amplitude is beyond the scope of the present work due to the complexity of the shock wave reflections. The existence of negative pressures in the wave is demonstrated by the observation of the cavitation cloud and of a second type of cavitation: the less frequent, and random, apparition of single bubbles that can be resolved optically (see Fig. 2 and [26]). Although cavitation in water is in principle possible at positive pressures below the vapor pressure of water ( $\approx 2.3$  kPa at  $20^\circ\text{C}$ ), water vapor bubbles in our experiment cannot be spontaneously generated at positive pressures. Even a bubble as big as the largest jet we used ( $30\ \mu\text{m}$  diameter) has a Laplace pressure ( $\approx 10$  kPa) that exceeds the vapor pressure and would collapse the bubble. Indeed, we did not observe cavitation bubbles in any of 13836 images recorded prior to the arrival of the XFEL pulse, such as the top image in Fig. 2.

The single cavitation bubbles that appear randomly in the pressure wave can be used to quantify the negative pressures present during their growth. The growth of a cavitation bubble in a liquid at negative pressures is described[51] by the Rayleigh-Plesset equation:

$$-\frac{(P_{ext} - P_b)}{\rho} = R \frac{\partial^2 R}{\partial t^2} + \frac{3}{2} \left( \frac{\partial R}{\partial t} \right)^2 + \frac{4\eta}{\rho R} \frac{\partial R}{\partial t} + \frac{2\sigma}{\rho R} \quad (5)$$

where  $R$  is the bubble radius,  $\rho$  the liquid density,  $P_b$  and  $P_{ext}$  the pressures in the bubble and in the surrounding liquid,  $\eta$  the liquid viscosity and  $\sigma$  its surface tension. For the conditions of our experiment, we can use the Rayleigh-Plesset equation to express an inequality for the maximum absolute value of the negative pressure,  $-P_{peak, negative}$ , that existed during the growth of the bubble (see [26] for derivation):

$$-P_{peak, negative} > \frac{3}{2}\rho(v_{est})^2 \quad (6)$$

where  $v_{est} = R(t_{image}) / (t_{image} - t_{S1})$  is a low estimate of the velocity with which the bubble grew, assuming it nucleated when the first shock was at the bubble location ( $t_{S1}$ ), and its radius was measured at  $t_{image}$ . Using this velocity estimate, the fastest growing bubble in our data had a radial expansion velocity of 126 m/s, corresponding to a negative pressure of at least  $-24$  MPa. This value is comparable to the ones that can be achieved in liquid water using techniques[10] that are not based on quartz crystal microinclusions or shock reflections.

The negative pressures that lead to the formation of the cavitation cloud are most likely larger than the ones at which single bubbles nucleate. Formation of a dense cavitation cloud was also encountered in shock reflection experiments in water in microfluidic channels[28] and the negative pressures were estimated at  $-60$  MPa for a system with similar shock pressures, time and length scales; we thus expect that comparable negative pressures generated the cavitation cloud in jets.

### E. Intensity and the sound pressure level of the cyclic pressure wave

The pressure wave in jets originates as a single cylindrical shock wave and eventually becomes a strongly attenuated multi-cycle pressure wave. Briefly between these limits, the wave is a cyclic propagating ultrasound that has very high amplitudes and intensities in the inner regions of the jet (the jet surface remains at the vacuum pressure). Since water in the cavitation cloud is no longer a single-phase liquid, we choose the initial moment for which the multiple-cycle wave forms as the moment when the first shock advances past the location of the maximum extent of the cavitation cloud. Figure 5 displays the maximum extent of the cavitation cloud along the jet, as symbols attached to the measured pressures. In all cases, the pressure of the first shock when it passes through the place where the last cavitation bubbles appear is within a factor of two of 100 MPa, and we will use a positive peak pressure of 100 MPa for further calculations. Since the negative pressures in the wave exceed  $-24$  MPa, the pressure waves have initial peak-to-peak pressures of at least 124 MPa, approximately twice the  $\approx 60$  MPa peak-to-peak pressures measured in experiments with focused ultrasonic waves[7]. We note that the focused ultrasound experiments reported in Ref. [11] might have exceeded 60 MPa peak-to-peak, because cavitation was observed at 24 MPa in water statically compressed to 20 MPa; assuming the pressure swings above and below the static pressure were equal ( $\pm 44$  MPa relative to 20 MPa), the peak-to-peak pressure was 88 MPa.

For a peak-to-peak pressure of 124 MPa, the corresponding peak-to-peak (pp) and root mean square (rms) sound pressure levels,  $L_{pp}$ , and  $L_{rms}$ , respectively, are given by

$$L_{pp} = 20 \log \frac{P_{pp}}{P_{ref}} \quad (7)$$

$$L_{rms} = 20 \log \frac{P_{rms}}{P_{ref}} \quad (8)$$

where  $P_{pp}$  is the peak-to-peak pressure,  $P_{rms}$  is the root mean square pressure, and  $P_{ref}$  is the reference pressure[52] of  $1 \mu\text{Pa}$  for sound in water, and  $20 \mu\text{Pa}$  for sound in air. According to Eq. 7,  $L_{pp}$  is at least 280 dB<sub>pp</sub> (re:  $1 \mu\text{Pa}$ ).  $L_{rms}$  cannot be calculated directly, but if we assume the pressure wave has a triangular profile (a common approximation of shock waveforms),  $L_{rms} = L_{pp} - 20 \log 2\sqrt{3} > 270$  dB<sub>rms</sub> (re:  $1 \mu\text{Pa}$ ), a thousand times more intense than the loudest sounds[3] produced by aquatic animals.

The cyclic pressure wave also has initially very large intensities. The instantaneous wave intensity  $I$ , given by

$$I = P_S u_p \quad (9)$$

is  $\approx 6$  GW/m<sup>2</sup> for a 100 MPa shock in water. Since the average intensity of a triangular waveform is three times smaller than the peak intensity, we estimate that the average wave intensity is on the order of 1 GW/m<sup>2</sup>. This is a very large sound intensity: a 1 GW/m<sup>2</sup> sound wave in air would have a sound intensity level of 210 dB (re:  $1 \text{ pW/m}^2$ ), larger than the strongest propagating sounds[4] measured in open atmosphere.

## F. Potential for damaging solid samples embedded in the jets

The very high amplitudes and intensities of the pressure wave launched in the jet are a potential impediment for experiments conducted at X-ray free-electron lasers with samples embedded in liquid jets. A new generation of X-ray laser facilities, such as the European XFEL (EuXFEL)[53, 54], will provide pulse repetition rates up to 4.5 MHz. To replenish samples at these rates, techniques to generate and characterize jets with  $\approx 100$  m/s velocities have been developed[55, 56], but even with such jets, at the 222 ns minimum pulse interval at EuXFEL, the probed regions will be only  $\approx 20$   $\mu\text{m}$  apart and may be subjected to pressures sufficiently large to damage carried samples, or modify the properties of the liquid through cavitation or shock heating.

While many crystalline materials retain their structural integrity at hydrostatic pressures above 1 GPa[57], shock waves apply initially an uniaxial compression and the shocked material can fail at lower stresses that are comparable to their engineering strengths. Depending on the compressive and tensile strengths of the sample, the damage could occur due to either the positive or the negative pressure swings. For example, a uniaxial tension of  $-24$  MPa is sufficient to fracture concrete[58] and rocks[59].

In our setup the first components exposed to the pressure waves were the nozzles generating the jet. We used nozzles (MicroFab Technologies, Inc.) made of borosilicate glass, which we inspected for damage after the experiments using an optical microscope (Zeiss Axio Imager.Z2m) at a resolution better than 1  $\mu\text{m}$ . None of the nozzles were damaged, which may seem surprising since glass is brittle. However, silicate glasses (*e.g.* fused silica, borosilicate and soda-lime glasses) are very hard materials due to their strong chemical bonds, and display high damage thresholds when exposed to shock waves. In silicate glasses, the stress thresholds for dynamic damage in compression (*i.e.*, the Hugoniot elastic limit), in tension (*i.e.*, the spall strength), or due to surface-nucleated cracks (*i.e.*, failure waves[60]), were all found to be above 1 GPa [60–62]. Since the distance between the X-ray beam and the nozzle must exceed several jet diameters to prevent the blocking of diffracted X-rays, our data shows that the peak wave pressures expected at the nozzle are below 100 MPa; this is more than one order of magnitude less than the shock damage thresholds of glass.

In the case of serial femtosecond crystallography (SFX)[63, 64] experiments done at X-ray lasers, protein microcrystals are being carried by liquid microjets into the interaction region. Protein crystals are soft materials because they are held together by weak intermolecular forces. To evaluate if they may be shock-damaged in SFX experiments, we use here the criterion that damage becomes possible if the pressure amplitude in the liquid is comparable or larger than the static compressive or tensile strength of the crystal, because the dynamic damage thresholds are not known for protein crystals. We also neglect changes in pressure as the wave refracts into the crystals; the pressure will increase in the crystals if their acoustic impedance is larger than the one of the liquid[34], which is for example the case of lysozyme crystals in water[65].

Data on the mechanical failure properties of protein crystals are scarce. To our knowledge, they have been investigated thoroughly only for lysozyme crystals, using micro indentation tests that measure their hardness[66, 67]. The lysozyme crystals are softer when more hydrated, and fully hydrated crystals (such as crystals carried in a water jet) had an indentation hardness in the range of 15–20 MPa. The relation between hardness and the compressive or tensile yield varies depending on the type of material, but the ultimate tensile strength is approximately three times smaller than hardness in many materials[68], and numerical simulations of lysozyme crystals found that the compressive yield stress is also approximately three times smaller than the hardness[69]. Therefore, we use here the criteria that lysozyme crystals may be damaged by the pressure wave if its amplitude is larger than 10 MPa. We note that the pressure amplitude limit for other protein crystals will be different and may be lower; for example, glucose isomerase crystals were found to be softer than lysozyme crystals[67].

The liquid jets used for high repetition rate SFX experiments will likely have 3–5  $\mu\text{m}$  diameters, several times thinner than the ones we investigated. Since experimental shock data does not exist for these thinner jets, we analyze here the potential for damage assuming that (i) the initial shock pressure is also on the order of 1 GPa and (ii) the pressure decay scales with the jet diameter the same way as in Fig. 5, because the initial pressure decay is associated with shock reflections and cavitation, whose dynamics scale with the jet diameter.

Excluding noisy data points, the pressure measurements shown in Fig. 5 exceed 10 MPa, which suggests that for an SFX experiment conducted with lysozyme crystals in aqueous microjets, using  $\approx 1$  mJ hard X-ray pulses focused to less than the jet diameter, crystals may be damaged if located up to at least 4 jet diameters away from the previous XFEL interaction region. The first SFX measurements made at the EuXFEL at a repetition rate of 1.1 MHz did not observe any degradation in the X-ray diffraction signal due to prior X-ray pulses[70, 71]. However, for these experiments we expect smaller pressure amplitudes than in our present data, because (i) the distance between jet regions probed by consecutive pulses was equal to at least 10 jet diameters, and (ii) the XFEL beam diameter was larger than the jet diameter. Shocks with a structure similar to the one we described here were observed when using an XFEL beam diameter of approximately half of the jet diameter, but for a beam  $\approx 3$  times larger than the jet, the shocks were barely visible and their structure could not be discerned[70].

Future SFX experiments at EuXFEL are projected to use X-ray beam sizes smaller than the jet diameter and up to

4.5 MHz repetition rates[72]. In this case, it will become necessary to ensure sufficient separation between consecutive regions along the jet, such that the pressure wave amplitude decays to values that do not affect the crystals. The data shown in Fig. 5 indicates that during propagation up to at least 2 jet diameters, the pressure decays exponentially and is reduced by an order of magnitude for every 1.5 jet diameters of travel. If this “short-range” decay law would continue to apply at longer propagation distances, a 1-GPa shock wave at  $0.5 D$  will decay to a 10-MPa pressure pulse at  $3.5 D$  and to a 1-MPa pulse at  $5 D$ ; these distances are approximately the same as the jet translation required to avoid the gap generated by a prior XFEL explosion in the jet[21, 56], therefore by using jets that are fast enough to avoid the gap, the shock damage would also be averted. However, at propagation distances longer than  $2\text{--}3 D$  the pressure decay law became less steep (see Fig. 5). Also, the short-range decay law is inconsistent with our observation of pressure waves at  $30 D$  in the 30-micron jets (see Fig. S3 in [26]), as it predicts incorrectly that the pressure amplitude should decay by almost 20 orders of magnitude.

To estimate the long-range attenuation of the shock, we can consider that after it generates multiple pressure oscillations, it becomes an ultrasonic wave. In water, ultrasound is attenuated with an exponential decay length inversely proportional to the square of the frequency[73]. Ultrasound approaching GHz frequencies is strongly attenuated in water, although not as rapidly as the shocks shown in Fig. 5. If the long-range attenuation of the wave is dominated by ultrasound absorption, in a  $30\text{-}\mu\text{m}$  jet the wave frequency will be  $\approx 0.1$  GHz according to Eq. 1, and a 10-fold pressure decay will occur in  $\approx 10$  mm, which is consistent with our observation[26] of pressure waves after  $\approx 1$  mm of propagation. In a  $3\text{-}\mu\text{m}$  diameter jet, such as the ones developed for SFX at the EuXFEL[56], the wave will have a frequency of  $\approx 1$  GHz, and its pressure will decrease 10-fold only after propagating for a distance of  $\approx 100 \mu\text{m}$ . This attenuation distance is longer than the spacing that can be produced by the fastest sample delivery jets[71] at 4.5 MHz repetition rates, thus crystal damage may occur at 4.5 MHz rates.

Given the lack of experimental data on the mechanical properties of various protein crystals investigated at XFELs, as well as on the propagation of the XFEL-induced pressure waves in liquid jets actually used for SFX, the existence and extent of crystal damage in MHz repetition rate SFX remains an open problem that requires further experimental investigations.

#### IV. CONCLUSIONS

A few-cycle, high intensity pressure wave with both positive and negative pressure peaks can be generated in free liquid microjets by launching a nanosecond shock wave along the jet. This ultrasound wave is an example of a multiple-cycle pressure wave with amplitudes as large as theoretically possible, because it is close to the limit of damaging its own medium through cavitation. The wave has a combination of remarkable properties including initial intensities on the order of  $1 \text{ GW/m}^2$ , frequencies in the near-gigahertz range, and large positive and negative peak pressures. It exhibits nonlinear features that are related to and yet distinct from similar phenomena observed in supersonic gas jets: self-generation of multiple trailing shocks that maintain their separation during propagation, a “Mach triangle” shock structure, and a varying frequency. Here we provided an initial description of these properties and of the basic physical mechanisms causing them, but further experiments, as well as simulations of shock reflections and cavitation[74–76], could provide new insights into the properties and dynamics of these waves.

Although our study required XFEL pulses focused to  $\approx 1 \mu\text{m}$  to initiate the pressure waves, we expect that similar waves can be generated using different excitation methods, in different liquids, and over a wider range of jet diameters. The main requirement is that the initial shock wave must have a spatial spread comparable to or smaller than the jet diameter, such that negative pressure reflections with large amplitudes can develop; with more spread pulses, these reflections could interfere destructively with the incoming positive pressure pulse. An initially cylindrical shock is not necessary, because the wave eventually adopts an axisymmetric shape; it may even be sufficient to generate the initial shock at the surface of the jet, similar to optical ablation experiments that produced shocks and cavitation in drops of opaque liquids[77–79].

Our data suggests that the jets can be as large as desired if a sufficiently strong initial shock can be applied. To generate waves in very thin jets, an ultrafast excitation in a very small region is needed. XFELs can be focused down to  $\approx 50$  nm beam diameters[80], but the size of the initially heated region depends on photoelectron diffusion[81] and electrostatic trapping[82], and may be larger than the beam size. If the heated region remains the same as the illuminated region, it may be possible to generate high-intensity cyclic pressure waves in jets down to 100 nm diameter, at frequencies above 10 GHz. Detection and characterization of such waves will however require new experimental techniques because the setup used here cannot resolve the contrast of shocks in jets with diameters below  $10 \mu\text{m}$ .

Although the high intensity of the pressure wave presents a challenge for certain XFEL experiments, it may enable other studies. For example, the wave could be used to induce and then study at atomic resolution the picosecond and nanosecond dynamics of shock damage[83] and tensile failure[84] in soft materials embedded in liquids. These waves also provide a new system for the study of cavitation in liquids. In the case of water, our observation of two

qualitatively distinct types of cavitation in the same system shows that apparently contradictory measurements of cavitation pressures[10, 20, 28] can be reconciled by the existence of two types of cavitation depending on how rapidly water is stretched; the pressure waves in jets are a system in which these types of cavitation can be investigated simultaneously to reveal their different mechanisms.

## ACKNOWLEDGMENTS

We thank Howard Stone and Francesco Grasso for helpful discussions. The experiments were supported by the U.S. Department of Energy, Office of Science, Chemical Sciences, Geosciences, and Biosciences Division. Data analysis and interpretation were primarily supported by startup funds from Rutgers University Newark. Use of the Linac Coherent Light Source (LCLS), SLAC National Accelerator Laboratory, is supported by the U.S. Department of Energy, Office of Science, Office of Basic Energy Sciences under Contract no. DE-AC02-76SF00515.

- 
- [1] J. M. Walsh and M. H. Rice, “Dynamic compression of liquids from measurements on strong shock waves,” *J. Chem. Phys.* **26**, 815–823 (1957).
- [2] J. C. Fisher, “The fracture of liquids,” *J. Appl. Phys.* **19**, 1062–1067 (1948).
- [3] B. Mohl, M. Wahlberg, P. T. Madsen, A. Heerfordt, and A. Lund, “The monopulsed nature of sperm whale clicks,” *J. Acoust. Soc. Am.* **114**, 1143–1154 (2003).
- [4] K. M. Eldred, Acoustic loads generated by the propulsion system, Report SP-8072 (National Aeronautics and Space Administration, 1971).
- [5] C. P. Lubert, “Sixty years of launch vehicle acoustics,” *Proc. Meet. Acoust.* **31**, 040004 (2017).
- [6] W. Lauterborn, T. Kurz, and I. Akhatov, “Nonlinear acoustics in fluids,” in Springer Handbook of Acoustics, edited by T. D. Rossing (Springer, Heidelberg, 2014) Book section 8, pp. 265–314, 2nd ed.
- [7] A. Arvengas, K. Davitt, and F. Caupin, “Fiber optic probe hydrophone for the study of acoustic cavitation in water,” *Rev. Sci. Instrum.* **82**, 034904 (2011).
- [8] Q. Zheng, D. J. Durben, G. H. Wolf, and C. A. Angell, “Liquids at large negative pressures: water at the homogeneous nucleation limit,” *Science* **254**, 829–832 (1991).
- [9] M. E. Azouzi, C. Ramboz, J. F. Lenain, and F. Caupin, “A coherent picture of water at extreme negative pressure,” *Nat. Phys.* **9**, 38–41 (2013).
- [10] F. Caupin, A. Arvengas, K. Davitt, M. E. Azouzi, K. I. Shmulovich, C. Ramboz, D. A. Sessoms, and A. D. Stroock, “Exploring water and other liquids at negative pressure,” *J. Phys. Cond. Mat.* **24**, 284110 (2012).
- [11] E. Herbert, S. Balibar, and F. Caupin, “Cavitation pressure in water,” *Phys. Rev. E* **74**, 041603 (2006).
- [12] Ya. B. Zeldovich and Yu. P. Raizer, Physics of shock waves and high-temperature hydrodynamic phenomena, 1st ed. (Academic Press, Waltham, MA, 1968).
- [13] L. F. Henderson, “General laws for propagation of shock waves through matter,” in Handbook of Shock Waves, Vol. 2, edited by G. Ben-Dor, O. Igra, and T. Elperin (Academic Press, San Diego, CA, 2001) p. 143.
- [14] D. E. Wilcox, A. Weir Jr., J. A. Nicholls, and R. Dunlap, “Location of Mach discs and diamonds in supersonic air jets,” *J. Aeronaut. Sci.* **24**, 150–152 (1957).
- [15] K. Matsuo, Y. Miyazato, and H. D. Kim, “Shock train and pseudo-shock phenomena in internal gas flows,” *Prog. Aerosp. Sci.* **35**, 33–100 (1999).
- [16] M. N. Liang, G. J. Williams, M. Messerschmidt, M. M. Seibert, P. A. Montanez, M. Hayes, D. Milathianaki, A. Aquila, M. S. Hunter, J. E. Koglin, D. W. Schafer, S. Guillet, A. Busse, R. Bergan, W. Olson, K. Fox, N. Stewart, R. Curtis, A. A. Miahnahri, and S. Boutet, “The Coherent X-ray Imaging instrument at the Linac Coherent Light Source,” *J. Synchrotron Radiat.* **22**, 514–519 (2015).
- [17] P. Emma, R. Akre, J. Arthur, R. Bionta, C. Bostedt, J. Bozek, A. Brachmann, P. Bucksbaum, R. Coffee, F.-J. Decker, Y. Ding, D. Dowell, S. Edstrom, A. Fisher, J. Frisch, S. Gilevich, J. Hastings, G. Hays, P. Hering, Z. Huang, R. Iverson, H. Loos, M. Messerschmidt, A. Miahnahri, S. Moeller, H. D. Nuhn, G. Pile, D. Ratner, J. Rzepiela, D. Schultz, T. Smith, P. Stefan, H. Tompkins, J. Turner, J. Welch, W. White, J. Wu, G. Yocky, and J. Galayda, “First lasing and operation of an ångstrom-wavelength free-electron laser,” *Nat. Photon.* **4**, 641–647 (2010).
- [18] S. M. Seltzer, “Calculation of photon mass energy-transfer and mass energy-absorption coefficients,” *Radiat. Res.* **136**, 147–170 (1993).
- [19] K. R. Beyerlein, H. O. Jonsson, R. Alonso-Mori, A. Aquila, S. Barty, A. Barty, R. Bean, J. E. Koglin, M. Messerschmidt, D. Ragazzon, D. Sokaras, G. J. Williams, S. Hau-Riege, S. Boutet, H. N. Chapman, N. Timneanu, and C. Caleman, “Ultrafast nonthermal heating of water initiated by an X-ray Free-Electron Laser,” *Proc. Natl. Acad. Sci. USA* **115**, 5652–5657 (2018).
- [20] C. A. Stan, P. R. Willmott, H. A. Stone, J. E. Koglin, M. Liang, A. L. Aquila, J. S. Robinson, K. L. Gumerlock, G. Blaj, R. G. Sierra, S. Boutet, S. A. H. Guillet, R. H. Curtis, S. L. Vetter, H. Loos, J. L. Turner, and F.-J. Decker, “Negative pressures and spallation in water drops subjected to nanosecond shock waves,” *J. Phys. Chem. Lett.* **7**, 2055–2062 (2016).

- [21] C. A. Stan, D. Milathianaki, H. Laksmono, R. G. Sierra, T. A. McQueen, M. Messerschmidt, G. J. Williams, J. E. Koglin, T. J. Lane, M. J. Hayes, S. A. H. Guillet, M. N. Liang, A. L. Aquila, P. R. Willmott, J. S. Robinson, K. L. Gumerlock, S. Botha, K. Nass, I. Schlichting, R. L. Shoeman, H. A. Stone, and S. Boutet, “Liquid explosions induced by X-ray laser pulses,” *Nat. Phys.* **12**, 966–971 (2016).
- [22] P. Kobel, D. Obreschkow, A. de Bosset, N. Dorsaz, and M. Farhat, “Techniques for generating centimetric drops in microgravity and application to cavitation studies,” *Exp. Fluids* **47**, 39–48 (2009).
- [23] T. Roth, W. Freund, U. Boesenberg, G. Carini, S. Song, G. Lefevvre, A. Goikhman, M. Fischer, M. Schreck, J. Grunert, and A. Madsen, “Pulse-resolved intensity measurements at a hard X-ray FEL using semi-transparent diamond detectors,” *J. Synchrotron Radiat.* **25**, 177–188 (2018).
- [24] P. A. Hart, S. Boutet, G. Carini, M. Dubrovin, B. Duda, D. Fritz, G. Haller, R. Herbst, S. Herrmann, C. J. Kenney, N. Kurita, H. Lemke, M. Messerschmidt, M. Nordby, J. Pines, D. Schafer, M. Swift, M. Weaver, G. Williams, D. Zhu, N. Van Bakel, and J. Morse, “The CSPAD megapixel x-ray camera at LCLS,” in *SPIE Optical Engineering + Applications*, edited by S. P. Moeller, M. Yabashi, and S. P. Hau-Riege (International Society for Optics and Photonics, 2012) p. 85040C.
- [25] S. Herrmann, G. Blaj, G. A. Carini, A. Dragone, D. Freytag, G. Haller, P. A. Hart, R. Herbst, C. J. Kenney, L. Manger, S. Nelson, S. Osier, J. Pines, M. Sikorski, S. Song, A. Tomada, and M. Weaver, “CSPAD upgrades at LCLS,” in *2013 IEEE Nuclear Science Symposium and Medical Imaging Conference (2013 NSS/MIC)* (IEEE, 2013) pp. 1–4.
- [26] Supplementary materials are available at [hyperlink to be generated]. They contain videos showing the generation and propagation of the waves, as well as a pdf file containing all shock propagation data, images of wave propagating at long distances, details of data smoothing, the derivation of Eq. (6), scaling of initial shock pressures with the pulse energy, the modeled temperature distribution inside the jets, and the procedures used to make the supplementary videos.
- [27] G. Blaj, M. Liang, A. L. Aquila, P. R. Willmott, J. E. Koglin, R. G. Sierra, J. S. Robinson, S. Boutet, and C. A. Stan, “Image data analyzed in “Generation of high-intensity ultrasound through shock propagation in liquid jets”,” Stanford Digital Repository, <https://purl.stanford.edu/cg924ym7624> (2019).
- [28] K. Ando, A. Q. Liu, and C. D. Ohl, “Homogeneous nucleation in water in microfluidic channels,” *Phys. Rev. Lett.* **109**, 044501 (2012).
- [29] W. Lauterborn and T. Kurz, “Physics of bubble oscillations,” *Rep. Prog. Phys.* **73**, 106501 (2010).
- [30] M. Arora, C. D. Ohl, and D. Lohse, “Effect of nuclei concentration on cavitation cluster dynamics,” *J. Acoust. Soc. Am.* **121**, 3432–3436 (2007).
- [31] E. Mach and P. Salcher, “Optische untersuchung der luftstrahlen,” *Ann. Phys.* **277**, 144–150 (1890).
- [32] M. L. Norman and K.-H. A. Winkler, “Supersonic jets,” *Los Alamos Science* **12**, 39–71 (1985).
- [33] G. A. Carlson and K. W. Henry, “Technique for studying dynamic tensile failure in liquids: application to glycerol,” *J. Appl. Phys.* **44**, 2201–2206 (1973).
- [34] L. F. Henderson, “On the refraction of shock waves,” *J. Fluid Mech.* **198**, 365–386 (1989).
- [35] R. R. Nourgaliev, S. Y. Sushchikh, T. N. Dinh, and T. G. Theofanous, “Shock wave refraction patterns at interfaces,” *Int. J. Multiphase Flow* **31**, 969–995 (2005).
- [36] We note that our Huygens-Fresnel construction provides only the shape of the front of the perturbation and not the wave intensity, which in general varies depending on the direction of propagation.
- [37] G. Pallares, M. E. Azouzi, M. A. Gonzalez, J. L. Aragones, J. L. F. Abascal, C. Valeriani, and F. Caupin, “Anomalies in bulk supercooled water at negative pressure,” *Proc. Natl. Acad. Sci. USA* **111**, 7936–7941 (2014).
- [38] G. Pallares, M. A. Gonzalez, J. L. F. Abascal, C. Valeriani, and F. Caupin, “Equation of state for water and its line of density maxima down to  $-120$  MPa,” *Phys. Chem. Chem. Phys.* **18**, 5896–5900 (2016).
- [39] V. Holten, C. Qiu, E. Guillerm, M. Wilke, J. Ricka, M. Frenz, and F. Caupin, “Compressibility anomalies in stretched water and their interplay with density anomalies,” *J. Phys. Chem. Lett.* **8**, 5519–5522 (2017).
- [40] W. J. Doebler and V. W. Sparrow, “Stability of sonic boom metrics regarding signature distortions from atmospheric turbulence,” *J. Acoust. Soc. Am.* **141**, EL592–EL597 (2017).
- [41] R. G. Jahn, “The refraction of shock waves at a gaseous interface,” *J. Fluid Mech.* **1**, 457–489 (1956).
- [42] M. H. Rice and J. M. Walsh, “Equation of state of water to 250 kilobars,” *J. Chem. Phys.* **26**, 824–830 (1957).
- [43] K. Nagayama, Y. Mori, K. Shimada, and M. Nakahara, “Shock Hugoniot compression curve for water up to 1 GPa by using a compressed gas gun,” *J. Appl. Phys.* **91**, 476–482 (2002).
- [44] P. C. Lysne, “A comparison of calculated and measured lowstress Hugoniot and release adiabats of dry and watersaturated tuff,” *J. Geophys. Res.* **75**, 4375–4386 (1970).
- [45] J. D. Smith, C. D. Cappa, W. S. Drisdell, R. C. Cohen, and R. J. Saykally, “Raman thermometry measurements of free evaporation from liquid water droplets,” *J. Am. Chem. Soc.* **128**, 12892–12898 (2006).
- [46] J. A. Sellberg, C. Huang, T. A. McQueen, N. D. Loh, H. Laksmono, D. Schlesinger, R. G. Sierra, D. Nordlund, C. Y. Hampton, D. Starodub, D. P. DePonte, M. Beye, C. Chen, A. V. Martin, A. Barty, K. T. Wikfeldt, T. M. Weiss, C. Caronna, J. Feldkamp, L. B. Skinner, M. M. Seibert, M. Messerschmidt, G. J. Williams, S. Boutet, L. G. Pettersson, M. J. Bogan, and A. Nilsson, “Ultrafast X-ray probing of water structure below the homogeneous ice nucleation temperature,” *Nature* **510**, 381–384 (2014).
- [47] C. Goy, M. A. C. Potenza, S. Dederà, M. Tomut, E. Guillerm, A. Kalinin, K. O. Voss, A. Schottelius, N. Petridis, A. Prosvetov, G. Tejada, J. M. Fernandez, C. Trautmann, F. Caupin, U. Glasmacher, and R. E. Grisenti, “Shrinking of rapidly evaporating water microdroplets reveals their extreme supercooling,” *Phys. Rev. Lett.* **120**, 015501 (2018).
- [48] C. A. Stan, G. F. Schneider, S. S. Shevkopyas, M. Hashimoto, M. Ibanescu, B. J. Wiley, and G. M. Whitesides, “A microfluidic apparatus for the study of ice nucleation in supercooled water drops,” *Lab on a Chip* **9**, 2293–2305 (2009).
- [49] J. P. Petitet, R. Tufeu, and B. Le Neindre, “Determination of the thermodynamic properties of water from measurements of

- the speed of sound in the temperature range 251.15 – 293.15 K and the pressure range 0.1 – 350 MPa,” *Int. J. Thermophys.* **4**, 35–50 (1983).
- [50] A. Savitzky and M. J. E. Golay, “Smoothing and differentiation of data by simplified least squares procedures,” *Anal. Chem.* **36**, 1627–1639 (1964).
- [51] M. S. Plesset and A. Prosperetti, “Bubble dynamics and cavitation,” *Annu. Rev. Fluid. Mech.* **9**, 145–185 (1977).
- [52] M. A. Breazeale and M. McPherson, “Physical acoustics,” in *Springer Handbook of Acoustics*, edited by T. D. Rossing (Springer, Heidelberg, 2014) Book section 8, pp. 215–246, 2nd ed.
- [53] M. Altarelli, “The European X-ray free-electron laser facility in Hamburg,” *Nucl. Instrum. Meth. B* **269**, 2845–2849 (2011).
- [54] M. Altarelli, “The European X-ray Free-Electron Laser: toward an ultra-bright, high repetition-rate x-ray source,” *High Power Laser Sci. Eng.* **3**, e18 (2015).
- [55] M. L. Grünbein, R. L. Shoeman, and R. B. Doak, “Velocimetry of fast microscopic liquid jets by nanosecond dual-pulse laser illumination for megahertz X-ray free-electron lasers,” *Opt. Express* **26**, 7190–7203 (2018).
- [56] M. O. Wiedorn, S. Awel, A. J. Morgan, K. Ayyer, Y. Gevorkov, H. Fleckenstein, N. Roth, L. Adriano, R. Bean, K. R. Beyerlein, J. Chen, J. Coe, F. Francisco Cruz-Mazo, T. Ekeberg, R. Graceffa, M. Heymann, D. A. Horke, J. Knoka, V. Mariani, R. Nazari, D. Oberthür, A. K. Samanta, R. G. Sierra, C. A. Stan, O. Yefanov, D. Rompotis, J. Correa, B. Erk, R. Treusch, J. Schulz, B. G. Hogue, A. M. Gan-Calvo, P. Fromme, J. Küpper, A. V. Rode, S. Bajt, R. A. Kirian, and H. N. Chapman, “Rapid sample delivery for megahertz serial crystallography at X-ray FELs,” *IUCrJ* **5**, 574–584 (2018).
- [57] A. Jayaraman, “Diamond anvil cell and high-pressure physical investigations,” *Rev. Mod. Phys.* **55**, 65–108 (1983).
- [58] D. W. Hobbs, “The tensile strength of rocks,” *Int. J. Rock Mech. Min. Sci.* **1**, 385–396 (1964).
- [59] M. F. M. Zain, H. B. Mahmud, A. Ilham, and M. Faizal, “Prediction of splitting tensile strength of high-performance concrete,” *Cement Concrete Res.* **32**, 1251–1258 (2002).
- [60] G. I. Kanel, S. V. Razorenov, A. S. Savinykh, A. Rajendran, and Z. Chen, “A study of the failure wave phenomenon in glasses compressed at different levels,” *J. Appl. Phys.* **98**, 113523 (2005).
- [61] C. S. Alexander, L. C. Chhabildas, and D. W. Templeton, “The Hugoniot elastic limit of soda-lime glass,” in *Shock Compression of Condensed Matter - 2007, Pts 1 and 2*, AIP Conference Proceedings, Vol. 955, edited by M. Elert, M. D. Furnish, R. Chau, N. C. Holmes, and J. Nguyen (2007) pp. 733–738.
- [62] M. J. Davis, “Laser-shock-induced spall and the intrinsic strength of glass,” *Int. J. Appl. Glass Sci.* **7**, 364–373 (2016).
- [63] H. N. Chapman, P. Fromme, A. Barty, T. A. White, R. A. Kirian, A. Aquila, M. S. Hunter, J. Schulz, D. P. DePonte, U. Weierstall, R. B. Doak, F. Maia, A. V. Martin, I. Schlichting, L. Lomb, N. Coppola, R. L. Shoeman, S. W. Epp, R. Hartmann, D. Rolles, A. Rudenko, L. Foucar, N. Kimmel, G. Weidenspointner, P. Holl, M. N. Liang, M. Barthelmeß, C. Caleman, S. Boutet, M. J. Bogan, J. Krzywinski, C. Bostedt, S. Bajt, L. Gumprecht, B. Rudek, B. Erk, C. Schmidt, A. Homke, C. Reich, D. Pietschner, L. Struder, G. Hauser, H. Gorke, J. Ullrich, S. Herrmann, G. Schaller, F. Schopper, H. Soltau, K. U. Kühnel, M. Messerschmidt, J. D. Bozek, S. P. Hau-Riege, M. Frank, C. Y. Hampton, R. G. Sierra, D. Starodub, G. J. Williams, J. Hajdu, N. Timneanu, M. M. Seibert, J. Andreasson, A. Røcker, O. Jonsson, M. Svenda, S. Stern, K. Nass, R. Andritschke, C. D. Schroter, F. Krasniqi, M. Bott, K. E. Schmidt, X. Y. Wang, I. Grotjohann, J. M. Holton, T. R. M. Barends, R. Neutze, S. Marchesini, R. Fromme, S. Schorb, D. Rupp, M. Adolph, T. Gorkhovev, I. Andersson, H. Hirsemann, G. Potdevin, H. Graafsma, B. Nilsson, and J. C. H. Spence, “Femtosecond X-ray protein nanocrystallography,” *Nature* **470**, 73–77 (2011).
- [64] S. Boutet, L. Lomb, G. J. Williams, T. R. M. Barends, A. Aquila, R. B. Doak, U. Weierstall, D. P. DePonte, J. Steinbrener, R. L. Shoeman, M. Messerschmidt, A. Barty, T. A. White, S. Kassemeyer, R. A. Kirian, M. M. Seibert, P. A. Montanez, C. Kenney, R. Herbst, P. Hart, J. Pines, G. Haller, S. M. Gruner, H. T. Philipp, M. W. Tate, M. Hromalik, L. J. Koerner, N. van Bakel, J. Morse, W. Ghonsalves, D. Arnlund, M. J. Bogan, C. Caleman, R. Fromme, C. Y. Hampton, M. S. Hunter, L. C. Johansson, G. Katona, C. Kupitz, M. N. Liang, A. V. Martin, K. Nass, L. Redecke, F. Stellato, N. Timneanu, D. J. Wang, N. A. Zatsepin, D. Schafer, J. DeFevers, R. Neutze, P. Fromme, J. C. H. Spence, H. N. Chapman, and I. Schlichting, “High-resolution protein structure determination by serial femtosecond crystallography,” *Science* **337**, 362–364 (2012).
- [65] S. Speziale, F. Jiang, C. L. Caylor, S. Kriminski, C.-S. Zha, R. E. Thorne, and T. S. Duffy, “Sound velocity and elasticity of tetragonal lysozyme crystals by Brillouin spectroscopy,” *Biophys. J.* **85**, 3202–3213 (2003).
- [66] H. Koizumi, H. Kawamoto, M. Tachibana, and K. Kojima, “Effect of intracrystalline water on micro-Vickers hardness in tetragonal hen egg-white lysozyme single crystals,” *J. Phys. D* **41**, 074019 (2008).
- [67] S. Tait, E. T. White, and J. D. Litster, “Mechanical characterization of protein crystals,” *Part. Part. Syst. Char.* **25**, 266–276 (2008).
- [68] P. Zhang, S. X. Li, and Z. F. Zhang, “General relationship between strength and hardness,” *Mat. Sci. Eng. A* **529**, 62–73 (2011).
- [69] A. Zamiri and S. De, “Modeling the mechanical response of tetragonal lysozyme crystals,” *Langmuir* **26**, 4251–4257 (2010).
- [70] M. L. Grünbein, J. Bielecki, A. Gorel, M. Stricker, R. Bean, M. Cammarata, K. Dörner, L. Fröhlich, L. Hartmann, S. Hauf, M. Hilpert, Y. Kim, M. Kloos, R. Letrun, M. Messerschmidt, G. Mills, G. Nass Kovacs, M. Ramilli, C. M. Roome, T. Sato, M. Scholz, M. Sliwa, J. Sztuk-Dambietz, M. Weik, B. Weinhausen, N. Al-Qudami, D. Boukhelef, S. Brockhauser, W. Ehsan, M. Emon, S. Esenov, H. Fangohr, A. Kaukher, T. Kluyver, M. Lederer, L. Maia, M. Manetti, T. Michelat, A. Münnich, F. Pallas, G. Palmer, G. Previtali, N. Raab, A. Silenzi, J. Szuba, S. Venkatesan, K. Wrona, Z. Zhu, R. B. Doak, R. L. Shoeman, L. Foucar, J.-P. Colletier, A. P. Mancuso, T. R. M. Barends, C. A. Stan, and I. Schlichting, “Megahertz data collection from protein microcrystals at an X-ray free-electron laser,” *Nat. Commun.* **9**, 3487 (2018).
- [71] M. O. Wiedorn, D. Oberthür, R. Bean, R. Schubert, N. Werner, B. Abbey, M. Aepfelbacher, L. Adriano, A. Allahgholi, N. Al-Qudami, J. Andreasson, A. Aplin, S. Awel, K. Ayyer, S. Bajt, I. Barák, S. Bari, J. Bielecki, S. Botha, D. Boukhelef, W. Brehm, S. Brockhauser, I. Cheviakov, M. Coleman, F. Cruz-Mazo, C. Danilevski, C. Darmanin, M. Domaracky,

- K. Dörner, Y. Du, H. Fangohr, H. Fleckenstein, M. Frank, P. Fromme, A. Gañán Calvo, Y. Gevorkov, K. Giewekemeyer, H. Ginn, H. Graafsma, R. Graceffa, D. Greiffenberg, L. Gumprecht, P. Göttlicher, J. Hajdu, S. Hauf, M. Heymann, S. Holmes, D. Horke, M. Hunter, S. Imlau, A. Kaukher, Y. Kim, A. Klyuev, J. Knoška, B. Kobe, M. Kuhn, C. Kupitz, J. Küpper, J. Lahey-Rudolph, T. Laurus, K. LeCong, R. Letrun, P. Lourdu Xavier, L. Maia, F. Maia, V. Mariani, M. Messerschmidt, M. Metz, D. Mezza, T. Michelat, G. Mills, D. Monteiro, A. Morgan, K. Muehlig, A. Munke, A. Münnich, J. Nette, K. Nugent, T. Nuguid, A. Orville, S. Pandey, G. Pena, P. Villanueva-Perez, J. Poehlsen, G. Previtali, L. Redecke, H. Rohde, A. Round, T. Safenreiter, I. Sarrou, T. Sato, M. Schmidt, B. Schmitt, R. Schönherr, J. Schulz, J. Sellberg, M. Seibert, C. Seuring, S. Shelby, R. Shoeman, M. Sikorski, A. Silenzi, C. A. Stan, X. Shi, S. Stern, J. Sztuk-Dambietz, J. Szuba, A. Tolstikova, M. Trebbin, U. Trunk, P. Vagovic, T. Ve, B. Weinhausen, T. White, K. Wrona, C. Xu, O. Yefanov, N. Zatsepin, J. Zhang, M. Perbandt, A. P. Mancuso, C. Betzel, and H. N. Chapman, “Megahertz serial crystallography,” *Nat. Commun.* **9**, 4025 (2018).
- [72] T. Tschentscher, C. Bressler, J. Grunert, A. Madsen, A. P. Mancuso, M. Meyer, A. Scherz, H. Sinn, and U. Zastrau, “Photon beam transport and scientific instruments at the European XFEL,” *Appl. Sci.* **7**, 592 (2017).
- [73] J. M. M. Pinkerton, “A pulse method for the measurement of ultrasonic absorption in liquids: results for water,” *Nature* **160**, 128–129 (1947).
- [74] E. Johnsen and T. Colonius, “Implementation of WENO schemes in compressible multicomponent flow problems,” *J. Comput. Phys.* **219**, 715–732 (2006).
- [75] X. X. Lyu, S. C. Pan, X. Y. Hu, and N. A. Adams, “Numerical investigation of homogeneous cavitation nucleation in a microchannel,” *Phys. Rev. Fluids* **3**, 064303 (2018).
- [76] S. Y. Grigoryev, B. V. Lakatos, M. S. Krivokorytov, V. V. Zhakhovsky, S. A. Dyachkov, D. K. Ilnitsky, K. P. Migdal, N. A. Inogamov, A. Y. Vinokhodov, V. O. Kompanets, Y. V. Sidelnikov, V. M. Krivtsun, K. N. Koshelev, and V. V. Medvedev, “Expansion and fragmentation of a liquid-metal droplet by a short laser pulse,” *Phys. Rev. Appl.* **10**, 064009 (2018).
- [77] M. S. Krivokorytov, A. Y. Vinokhodov, Y. V. Sidelnikov, V. M. Krivtsun, V. O. Kompanets, A. A. Lash, K. N. Koshelev, and V. V. Medvedev, “Cavitation and spallation in liquid metal droplets produced by subpicosecond pulsed laser radiation,” *Phys. Rev. E* **95**, 031101(R) (2017).
- [78] M. S. Krivokorytov, Q. Zeng, B. V. Lakatos, A. Y. Vinokhodov, Y. V. Sidelnikov, V. O. Kompanets, V. M. Krivtsun, K. N. Koshelev, C. D. Ohl, and V. V. Medvedev, “Shaping and controlled fragmentation of liquid metal droplets through cavitation,” *Sci. Rep.* **8**, 597 (2018).
- [79] D. Kurilovich, T. F. Pinto, F. Torretti, R. Schupp, J. Scheers, A. S. Stodolna, H. Gelderblom, K. S. E. Eikema, S. Witte, W. Ubachs, R. Hoekstra, and O. O. Versolato, “Expansion dynamics after laser-induced cavitation in liquid tin microdroplets,” *Phys. Rev. Appl.* **10**, 054005 (2018).
- [80] H. Mimura, H. Yumoto, S. Matsuyama, T. Koyama, K. Tono, Y. Inubushi, T. Togashi, T. Sato, J. Kim, R. Fukui, Y. Sano, M. Yabashi, H. Ohashi, T. Ishikawa, and K. Yamauchi, “Generation of  $10^{20}$  W/cm<sup>-2</sup> hard x-ray laser pulses with two-stage reflective focusing system,” *Nat. Commun.* **5**, 3539 (2014).
- [81] R. Sanishvili, D. W. Yoder, S. B. Pothineni, G. Rosenbaum, S. L. Xu, S. Vogt, S. Stepanova, O. A. Makarov, S. Corcoran, R. Benn, V. Nagarajan, J. L. Smith, and R. F. Fischetti, “Radiation damage in protein crystals is reduced with a micron-sized X-ray beam,” *Proc. Natl. Acad. Sci. USA* **108**, 6127–6132 (2011).
- [82] S. P. Hau-Riege, “Photoelectron dynamics in X-ray free-electron-laser diffractive imaging of biological samples,” *Phys. Rev. Lett.* **108**, 238101 (2012).
- [83] C. E. Wehrenberg, D. McGonegle, C. Bolme, A. Higginbotham, A. Lazicki, H. J. Lee, B. Nagler, H. S. Park, B. A. Remington, R. E. Rudd, M. Sliwa, M. Suggit, D. Swift, F. Tavella, L. Zepeda-Ruiz, and J. S. Wark, “In situ X-ray diffraction measurement of shock-wave-driven twinning and lattice dynamics,” *Nature* **550**, 496–499 (2017).
- [84] B. Albertazzi, N. Ozaki, V. Zhakhovsky, A. Faenov, H. Habara, M. Harmand, N. Hartley, D. Ilnitsky, N. Inogamov, Y. Inubushi, T. Ishikawa, T. Katayama, T. Koyama, M. Koenig, A. Krygier, T. Matsuo, S. Matsuyama, E. McBride, K. P. Migdal, G. Morard, H. Ohashi, T. Okuchi, T. Pikuz, N. Purevjav, O. Sakata, Y. Sano, T. Sato, T. Sekine, Y. Seto, K. Takahashi, K. Tanaka, Y. Tange, T. Togashi, K. Tono, Y. Umeda, T. Vinci, M. Yabashi, T. Yabuuchi, K. Yamauchi, H. Yumoto, and R. Kodama, “Dynamic fracture of tantalum under extreme tensile stress,” *Sci. Adv.* **3**, e1602705 (2017).